scientific reports

Check for updates

OPEN

Strain tuning of optical and thermoelectric properties of monolayer BAs

Raad Chegel

This study investigates the electronic, optical and thermoelectric properties of monolayer boron arsenide (BAs) using a fifth-nearest-neighbor tight-binding model based on density functional theory (DFT) calculations, with a particular focus on the effects of biaxial strain to tune its characteristics for optoelectronic and thermoelectric applications. The results show that monolayer BAs possesses a direct band gap of approximately 1.2 eV at the K-point, maintaining its semiconducting nature across a strain range of − 8% to + 8%. The band gap is observed to decrease under compressive strain and increase under tensile strain. Optical spectra exhibit two distinct peaks in the infrared and ultraviolet regions, corresponding to transitions between the valence and conduction bands at the K and M points, which are significantly modulated by strain. Specifically, compressive strain induces a red-shift in these optical peaks, while tensile strain causes a blue-shift. The strain-dependent electronic modifications also significantly influence the thermoelectric properties of BAs, leading to enhancing under compressive strain and decreasing with tensile strain.

Keywords Monolayer BAs, Optical properties, Strain, Thermoelectric

Two-dimensional materials have garnered significant attention in recent years due to their unique physical properties and broad applicability across diverse fields, including electronics, thermoelectric, optoelectronics, and photovoltaics[1–3]. The emergence of 2D materials has led to significant improvements and numerous innovations in scientific research and industrial applications. Among these materials, graphene is the most well-known and widely studied member, having been extensively examined experimentally[4–6]. Graphene is composed of carbon atoms arranged in a hexagonal planar structure and exhibits remarkable electronic properties[7]. Notable features of graphene include its linear energy–momentum relationship near the Dirac point and a zero-energy gap at the K-point, resulting from the contact between valence and conduction bands[8]. This configuration leads to the presence of massless Dirac fermions at the K-point, enabling tunable energy modulation and highlighting graphene's promising potential in electronic-based devices[9,10]. The absence of an intrinsic band gap in graphene limits its application, particularly in transistors and other logic devices[11]. However, this limitation can be addressed through various techniques, such as introducing dopants, forming heterostructures, applying strain or creating graphene-based nanotubes[12–15]. These approaches allow for band gap engineering, enabling graphene to be tailored for a broader range of electronic and optoelectronic applications[16–18].

Beyond graphene, researchers have extensively investigated numerous two-dimensional materials with graphene-like structures, including Silicene, Germanene, boron nitride (BN), silicon carbide (SiC) and boron phosphide (BP)[19–25]. Among these, elemental structures like silicene and germanene feature buckled configurations and possess a zero-band gap at the Dirac point, which can be tuned through applied bias voltage[20,26–28]. Two-dimensional materials with planar structures and different atomic elements exhibit distinct electronic properties compared to graphene, including non-zero band gaps[29]. This characteristic stems from the difference in electronegativity between constituent atoms, making these materials particularly suitable for applications requiring tunable electronic properties[18,30]. Two-dimensional III-V materials have attracted significant attention due to their direct band gaps and diverse photoelectric properties, which make them suitable for applications in optical devices, piezoelectric systems, and infrared sensors[31,32]. Phonon dispersion spectrum analysis has confirmed that monolayer BAs exhibits dynamic stability[33]. Moreover, BAs monolayers exhibit a direct band gap of approximately 0.9 eV at the K point[34] and demonstrate high carrier mobility comparable to graphene, which notably increases under compressive strain[35]. BAs exhibits a smaller energy gap compared to other III-V materials such as monolayer BN and BP and this characteristic potentially leads to higher electrical conductivity and enhanced thermoelectric applications[36]. Its band structure and electrical properties are sensitive to parameters such as impurities and strain. Both tensile and compressive biaxial strain

Department of Physics, Faculty of Science, Razi University, Kermanshah, Iran. email: raad.chegel@gmail.com

induce significant modifications in its band structure[37]. DFT studies have revealed that the energy gap increases under tensile strain and decreases under compressive strain[37,38]. These effects also induce blue- and red-shifts in the optical properties of the BAs monolayer, optimizing its thermoelectric performance[39].

It is noteworthy that applying strain to 2D materials induces remarkable properties, as demonstrated in various studies[40–42]. For instance, the initially unstable Si_2C monolayer becomes dynamically stable under a 2.5% tensile strain and fluorination, with its band gap varying with strain[43]. Similarly, monolayer boron pnictides exhibit strong optical absorption in the visible and near-infrared ranges, with enhanced photocatalytic properties under strain[44]. The monolayer Ga_2TeS also shows improved visible-light absorption with strain[45]. Additionally, SiC_2, known for superior absorption in the near-infrared and visible regions, displays a significant red-shift in its optical peaks under strain[46].

The electrical properties of this material are highly sensitive to external factors; for instance, introducing vacancies induces magnetic moments, while the presence of certain defects cases a semiconductor-to-metal transition[47,48]. Additionally, through appropriate doping, BAs can be engineered into a spin-polarized semiconductor, offering potential for applications in next-generation electronics, spintronics, and optoelectronics[49]. Studies have demonstrated that the adsorption capacity of alkali atoms (Li, Na, and K) on BAs is comparable to that of graphene and similar related materials and with excellent storage potential for these elements, BAs undergoes a semiconducting-to-metallic transition, leading to enhanced conductivity[50]. The monolayer BAs also exhibits effective gas adsorption properties, with demonstrated applications in the adsorption of gases such as NO_2 and NO[51]. Additionally, BAs has been identified as a promising gas sensor for SO_2, with acceptable sensitivity levels[52]. Hydrogen adsorption on monolayer BAs induces a spin-polarized semiconducting nature and creates a significant magnetic moment, increasing its potential for sensing and magnetic applications[53]. Optical studies of BAs reveal a pronounced anisotropy and strong absorption in the visible–UV range[54]. The BAs structure can also exhibit modified electrical and optical properties when incorporated into heterostructures with various other materials[55–57]. Furthermore, BAs retains its semiconducting nature when cut into nanoribbons, with its band gap becomes width-dependent, providing further tunability for nanoelectronic applications[54].

This study investigates the properties of monolayer BAs, illustrating that biaxial strain is an effective approach for modifying and tuning its electronic, optical, and thermoelectric characteristics. For this purpose, initially, the required hopping parameters for the tight binding model are obtained from DFT calculations. Subsequently, the band structure and optical dipole matrix elements for the allowed transitions are explored and then the effects of the strain on the optical properties of BAs are investigated. Finally, through investigation of thermal properties, the study demonstrates that strain parameters can significantly influence the thermoelectric properties of BAs.

Model and formalism

To investigate the electronic and optical properties of monolayer BAs, a fifth-nearest-neighbor tight-binding model is employed to construct the Hamiltonian matrix for monolayer BAs, ensuring close agreement with Density Functional Theory (DFT) calculations. The structure of monolayer BAs includes two nonequivalent atoms, boron (B) and arsenic (As), in the primitive unit cell. Using second quantization, we can express the Hamiltonian in terms of the creation and annihilation operators as follow[25]:

$$[\mathrm{H}]^{(\alpha,\beta)} = \delta_{\alpha\beta}\varepsilon_{\alpha}^{(0)}\sum_{\mathrm{p}} \mathrm{c}_{\mathrm{p}}^{\dagger}(\alpha)\, c_{\mathrm{p}}(\alpha) + \sum_{v=1}^{3}\sum_{<\mathrm{p,q}>} \mathrm{t}_{\mathrm{pq}}^{(v)}(\alpha,\beta)\mathrm{c}_{\mathrm{p}}^{\dagger}(\alpha)\, c_q(\beta) \tag{1}$$

which $\delta_{\alpha\beta}$ represents the Kronecker delta and the operators $\mathrm{c}_{\mathrm{p}}^{\dagger}(\alpha)$ and $c_{\mathrm{p}}(\alpha)$ are the creation and annihilation operators for an electron at the p-th unit cell on the sublattice with atom type α. $\mathrm{t}_{\mathrm{pq}}^{(m)}(\alpha,\beta)$ denotes the m -th nearest-neighbor hopping integral between α and β type atoms at unit cells p and q, respectively. In this study, these hopping parameters are denoted as (t_1, t_2, t_3, t_4), corresponding to the first through fifth nearest neighbors ($m = 1, 2, 3, 4$). Furthermore, $\varepsilon_{\alpha}^{(0)}$ represents the on-site energy of an α atom, which appears along the main diagonal of the Hamiltonian matrix.

So far, no theoretical study has been conducted on the opto-electronic properties of monolayer BAs, making it necessary to calculate the required parameters for the tight-binding model, including the hopping integrals and on-site energies. To ensure accuracy of the theoretical model, the required parameters are carefully determined by fitting the tight-binding results to Density Functional Theory (DFT) calculations. Table 1 provides a detailed list of these parameters.

The Hamiltonian matrix elements describe interactions between neighboring atoms at α and β sites and can be expressed in terms of hopping integrals $[t_{\mathrm{m}}]$ and on-site energy $[\Delta_{\alpha}]$ parameters. The diagonal elements $(H_{\alpha\alpha})$ represent coupling between atoms on α sites, including self-coupling and second-nearest neighbor interactions. The off-diagonal elements $[H_{\alpha\beta}]$ describe coupling between α and β sites, which includes first to fifth nearest neighbor interactions. These matrix elements are expressed as[20]:

Structure	t_1	t_2	t_3	t_4	t_5
BAs	2.016	0.189	0.16	0.027	0.067

Table 1. The 5-th nearest-neighbor tight-binding hopping parameters for monolayer BAs.

$$H_{\alpha\alpha}(\boldsymbol{k}) = \Delta_\alpha + \sum_{m=2,5} t_m F_m(\boldsymbol{k})$$
$$H_{\alpha\beta}(\boldsymbol{k}) = \sum_{m=1,3,4} t_m F_m(\boldsymbol{k}) \quad (2)$$

Here, $F_m(\boldsymbol{k}) = \sum_{\boldsymbol{d}_m} e^{-i\boldsymbol{k}.\boldsymbol{d}_v}$ and $\boldsymbol{d}_m$ represent the distance between the origin atom and its first through fifth neighboring atoms. The wave vector $\boldsymbol{k}$ can be expressed in terms of the continuous wave vector as $\boldsymbol{k} \equiv (k_x, k_y)$.

Using this Hamiltonian, the band structure can be calculated through the tight-binding method. The band structure $E_{2D}^{(l)}(\boldsymbol{k})$ of monolayer BAs for the valence and conduction bands ($l = c, v$) is obtained by solving the Schrödinger equation $H(\boldsymbol{k})C(\boldsymbol{k}) = E_{2D}^{(l)}(\boldsymbol{k})C(\boldsymbol{k})$, where $\boldsymbol{k}$ is the wave vector and $C(\boldsymbol{k})$ represents the expansion coefficients. In matrix form and $\boldsymbol{k}$-space, the Schrödinger equation is written as[16]:

$$\begin{pmatrix} H_{\alpha\alpha} & H_{\alpha\beta} \\ H_{\beta\alpha} & H_{\beta\beta} \end{pmatrix} \begin{pmatrix} C_\alpha^l(\boldsymbol{k}) \\ C_\beta^l(\boldsymbol{k}) \end{pmatrix} = E_{2D}^{(l)}(\boldsymbol{k}) \begin{pmatrix} C_\alpha^l(\boldsymbol{k}) \\ C_\beta^l(\boldsymbol{k}) \end{pmatrix} \quad (3)$$

Using the parameters from Table 1, the tight binding band structure [dashed blue lines] is plotted in Fig. 1(a) and compared with DFT [hybrid HSE06 approximation] results [green lines]. The tight binding shows excellent agreement, particularly in reproducing the correct band gap when compared with our DFT calculations and previous studies. Given this strong agreement, this Hamiltonian formulation serves as a powerful tool for investigating various properties of BAs, including its electronic structure, transport properties, and other physical phenomena.

This study investigates the effects of strain on various properties of monolayer BAs. When strain is applied to the structure, the distances between B and As atoms and their bond angles change. These modifications, in turn, alter the hopping parameters t_m, due to their dependence on the displacement vector between neighboring atoms (up to fifth neighbors).

The functional dependence of hopping parameter changes on strain can be described using Harrison's relation, which has been widely employed in numerous studies. In this relationship, the hopping integral parameters between i-th neighbors in the absence and presence of strain are denoted as $t'_m = t_m \frac{l'^2_m}{l^2_m}$, respectively[58]. Furthermore, l_m and l'_m denote the distances between i-th neighboring atoms without and with strain, respectively.

Based on linear elasticity, the relationship between atomic positions under strain can be written as:

$$\boldsymbol{r}'_i = \begin{pmatrix} 1+\epsilon_x & 0 \\ 0 & 1+\epsilon_y \end{pmatrix} \boldsymbol{r}_i \quad (4)$$

where $\epsilon_x = \epsilon$ represents biaxial strain applied along zigzag $\widehat{x}$ direction, while $\epsilon_y = \epsilon$ corresponds to strain applied in the armchair $\widehat{y}$ direction. In these calculations, the parameter ϵ is defined as the ratio of the deformed bond length to the original bond length. The positive and negative values of ϵ indicate tensile and compressive strain, respectively. One result of this modification in the hopping integrals is the induced changes in the Hamiltonian of the BAs structure which directly influences its electronic and optical properties. For the case of biaxial strain, equal bond length changes occur in both the armchair and zigzag directions, preserving the hexagonal symmetry

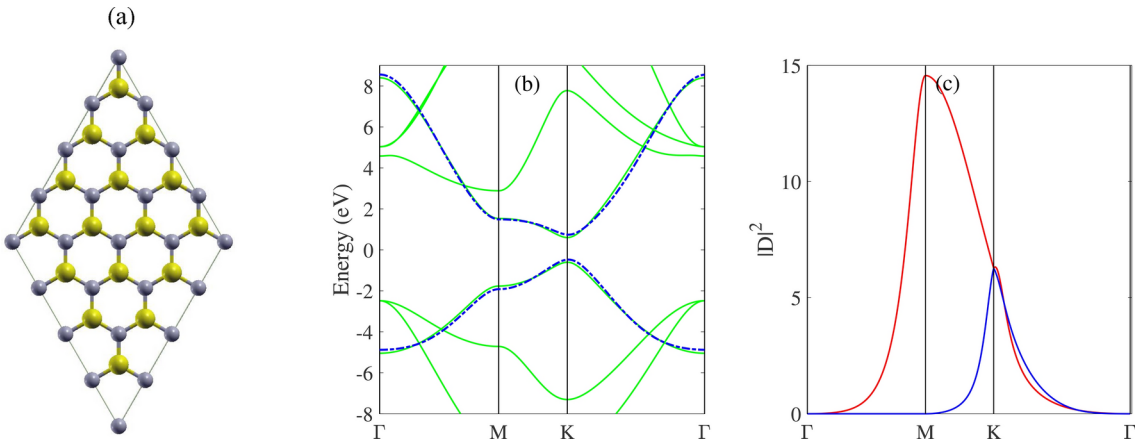

Fig. 1. (**a**) Schematic representation of the monolayer BAs. (**b**) Band structure of monolayer BAs calculated using the tight-binding model (dashed lines) compared with DFT results (solid lines). The direct band gap at the K-point is approximately 1.2 eV, which is constant in both methods. (**c**) The behavior of the $|D|^2$ as a function of the wave vector along the Γ-M-K-Γ path for both x and y directions.

of the BAs structure. Consequently, the first Brillouin zone undergoes symmetric modifications proportional to the strain parameter ϵ.

In addition to hopping parameters, the onsite energies Δ_α in the tight-binding Hamiltonian of monolayer BAs can vary with applied strain, directly influencing the diagonal elements of the Hamiltonian matrix. This strain dependence aligns with previous studies on graphene and monolayer BP, underscoring its relevance across 2D materials[59,60]. In this study, these changes are modeled as functions of the applied strain, enabling a detailed description of the electronic structure under deformation. Specifically, the on-site energies can be expressed as:

$$\Delta_\alpha(\epsilon) = \pm \sum_{i=0}^{2} \eta_i \left(\frac{\epsilon_x + \epsilon_x}{2} \right)^i \tag{5}$$

where η_i are fitting coefficients. These onsite energies $\Delta_\alpha(\epsilon)$ are determined by matching the tight binding band structure to DFT results, ensuring consistency between the two methods. The resulting coefficients for monolayer BAs under biaxial strain, obtained from this renormalization, are $\eta_i = [1.20, 3.21, -13.27]$. This approach not only validates the tight binding model against DFT but also provides a parameterized framework for strain effects, offering a valuable tool for future theoretical investigations of BAs and related 2D systems. In this study, the effects of tensile and compressive strain within a range of ± 12% are examined, a range in which multiple studies have demonstrated the dynamic stability of the monolayer BAs structure[37,39,54]

Investigation the optical properties of BAs requires calculation the dipole matrix elements. For this purpose, based on the obtained band structure, the allowed transitions between the valence and conduction bands [(v) and (c)] can be identified by computing the interband optical matrix elements $\boldsymbol{D}(\boldsymbol{k}) = \langle \Psi^{\mathrm{f}}_{\boldsymbol{k}}(\boldsymbol{r}) | \nabla | \Psi^{\mathrm{i}}_{\boldsymbol{k}}(\boldsymbol{r}) \rangle$, where the initial $[\Psi^i]$ and final $[\Psi^f]$ wave functions are derived from the gradient of the Hamiltonian operator[61].

The interband dipole matrix elements are defined as follows[61,62]:

$$D(\boldsymbol{k}) = \frac{1}{N} \sum_{\alpha,\beta} \sum_{\boldsymbol{d}_m} C^{(c)*}_\alpha(\boldsymbol{k}) C^{(v)}_\beta(\boldsymbol{k}) e^{-i\boldsymbol{k}.\boldsymbol{d}_m} \boldsymbol{d}_m \langle \phi(\boldsymbol{r}) | H(\boldsymbol{k}) | \phi(\boldsymbol{r} - \boldsymbol{d}_m) \rangle \tag{6}$$

where in this equation, $\phi(\boldsymbol{r} - \boldsymbol{d}_m)$ represents the p_z-orbital atomic wave function of the different atoms in the structure and $\boldsymbol{d}_m$ is the distance between the origin atom and its m-th neighboring atoms. By combining the band structure and the dipole matrix elements, the optical properties of monolayer BAs can be calculated.

Generally, the optical properties are evaluated using the frequency-dependent complex dielectric function, expressed as $\varepsilon(\omega) = \varepsilon_1(\omega) + i\varepsilon_2(\omega)$. The imaginary part $\varepsilon_2(\omega)$ of dielectric function is calculated from the momentum matrix elements between the occupied and unoccupied wave functions, following selection rules[20]:

$$\varepsilon_2(\omega) = \frac{2e^2\pi}{\Omega\varepsilon_0} \int |\mathrm{d}(\boldsymbol{k})|^2 \frac{E^{cv}(\boldsymbol{k})}{[E^{cv}(\boldsymbol{k})]^2 - [\hbar\Omega]^2} d\boldsymbol{k} \tag{7}$$

Here, the complex frequency $\Omega = \omega + i\Gamma_0$ depends on the photon frequency ω and broadening parameter Γ_0 and ε_0 represents the dielectric constant of free space. T The integration is performed over the first Brillouin zone wave vectors. The $\boldsymbol{k}$ dependence of electric dipole moment $\mathrm{d}(\boldsymbol{k})$ for transition between valence and conduction bands, with energy difference $E^{cv}(\boldsymbol{k})$ is defined by $\mathrm{D}(\boldsymbol{k}) = \left(\frac{m_e}{\hbar e}\right) E^{cv}(\boldsymbol{k})\ \mathrm{d}(\boldsymbol{k})$. The real part $\varepsilon_1(\omega)$ is then calculated by the Kramers–Kronig relation. The expressions of the refraction index $n(\omega)$ can be derived from the real and imaginary components $\varepsilon(\omega)$ of the dielectric function as follows:

$$n(\omega) = \frac{1}{2} \left[\sqrt{\varepsilon_1(\omega)^2 + \varepsilon_2(\omega)^2} + \varepsilon_1(\omega)^2 \right]^{\frac{1}{2}} \tag{8}$$

To investigate the thermoelectric properties in relation to the chemical potential μ, the transport coefficients $\Theta_{qq'}(\mu)$ are characterized by the following expressions[63]:

$$\Theta_{qq'}(\mu) = \int d\varepsilon \left[\frac{-\partial f(\varepsilon - \mu)}{\partial \varepsilon} \right] (\varepsilon - \mu)^{q+q'-2} \alpha(\varepsilon) \tag{9}$$

The spectral conductivity $\alpha(\varepsilon)$ can be expressed in terms of the velocity operator $\boldsymbol{\nu}^{(l)}_{\boldsymbol{k}} = \nabla_{\boldsymbol{k}} E^{(l)}(\boldsymbol{k})$ and the spectral function $A_p(\boldsymbol{k}, \varepsilon)$, which corresponds to the p-th eigenvalue of the Hamiltonian, as[64]:

$$\alpha(\varepsilon) = \sum_{\boldsymbol{k}, l=c,v} \left(\nu^{(l)}_{\boldsymbol{k}} A_p(\boldsymbol{k}, \varepsilon) \right)^2 \tag{10}$$

Using these transport coefficient expressions, the dependence of various thermoelectric properties on μ can be defined. The thermal conductivity $\kappa(\mu)$, thermoelectric figure-of-merit $ZT(\mu)$, Lorenz number $L(\mu)$ and Power factor $\mathrm{PF}(\mu)$ are derived in terms of the transport coefficients $\Theta_{qq'}(\mu)$, as follows[25,64,65]:

$$\kappa(\mu) = \frac{k_B^2}{T}\left[\frac{\Theta_{22}(\mu)\Theta_{11}(\mu) - \Theta_{12}(\mu)\Theta_{21}(\mu)}{\Pi_{11}(\mu)}\right]$$

$$ZT(\mu) = \frac{[\Theta_{12}(\mu)]^2}{\Theta_{11}(\mu)\Theta_{22}(\mu) - [\Theta_{12}(\mu)]^2}$$

$$L(\mu) = \frac{\Theta_{11}(\mu)\Theta_{22}(\mu) - \Theta_{12}^2(\mu)}{T^2\Theta_{11}^2(\mu)}$$

$$PF(\mu) \equiv \frac{[\Theta_{12}(\mu)]^2}{T^2\Theta_{11}(\mu)}$$

Results and discussions

Optical properties

Figure 1 illustrates the band structure of monolayer BAs along the high symmetric path Γ-M-K-Γ in the Brillouin zone. The results obtained from tight-binding model (shown in blue dashed lines) are compared with those from the DFT calculations (depicted in green). According to our DFT calculations, the optimized BAs structure exhibits a lattice constant of a = 3.36 Å and a B-As bond length of 1.94 Å, consistent with previous DFT studies[33].

In the employed tight-binding model, the focus is on analyzing the behavior of the highest occupied molecular orbital (LUMO) and lowest unoccupied molecular orbital (HOMO), which are highlighted in the Fig. 1(b). The asymmetry of these two bands relative to the Fermi level arises from the use of the tight-binding model with a fifth-nearest-neighbor approximation. The tight binding results show that this structure has a direct band gap of approximately 1.2 eV at the K point consistent with previous DFT results[37]. This band gap leads to parabolic band dispersion for valence and conduction bands around the K point. Additionally, the distance between the valence and conduction bands at M point is approximate 3.4 eV.

One of the main goals of this study is to investigate the optical properties of the monolayer BAs. For this purpose, we investigated the dipole matrix elements, which represent the allowed transitions between valence and conduction bands at various points in the Brillouin zone. Figure 1(c) illustrates the behavior of the $|D|^2$ as a function of the wave vector along the Γ-M–K-Γ path for both x and y directions. The intensity of the $|D|$ is negligible around the Γ point and by moving away from this point, it increases until reaching the maximum peak values at K and M points, with a higher intensity observed at the M point. Along the Γ – M path, the y-direction has zero intensity while the x-direction reaches a peak at the M point. Conversely, along the M–K path, the intensity in the x-direction decreases while it increases in the y-direction. Ultimately, both directions reach peaks with the same intensity at the K point. Along the K-Γ path, the x and y directions display similar behavior, with a nonlinear reduction in intensity relative to the wave vector. These results indicate that the |D| in the x-direction depends more strongly on the wave vector compared to the y-direction. This suggests that the optical transitions between the valence and conduction bands occur at the K and M points, leading to the appearance of peaks in the optical spectrum of monolayer BAs.

To illustrate the effects of strain parameters on the electrical properties of BAs, Fig. 2 shows the DOS spectrum for BAs under different tensile and compressive strain values. In the absence of strain, the DOS spectrum exhibits two peaks on both sides of the Fermi level due to Van Hove singularities associated with the band edges.

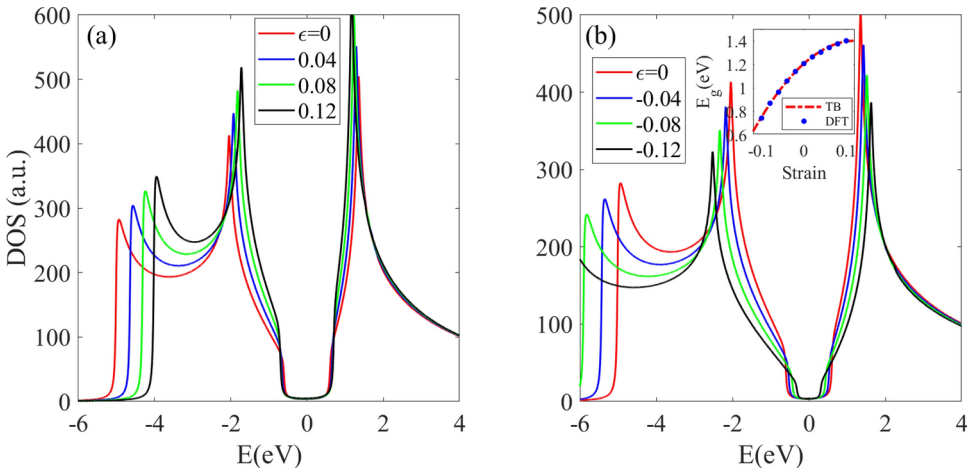

Fig. 2. Strain-dependent DOS spectra with (**a**) compressive and (**b**) tensile strains, respectively. compressive strain shifts peaks closer to the Fermi level, while tensile strain shifts them further. Inset (**b**) Band gap variation in monolayer BAs under compressive and tensile strains from − 8% to + 8%. Compressive strain decreases the band gap, while tensile strain increases it.

Additionally, due to the presence of a nonzero band gap, the DOS exhibits a zero-intensity region between the highest occupied state and the lowest unoccupied state, corresponding to the band gap.

Applying strain directly affects the position and intensity of the DOS peaks on both sides of the Fermi level, as well as the band gap region. Specifically, under tensile strain, the peaks shift towards the Fermi level, reaching energies of – 1.72 eV and 1.2 eV for approximately 12% strain. Conversely, for compressive strain, the DOS peaks move away from the Fermi level, reaching – 2.5 eV and 1.62 eV for approximately – 12% strain. Another notable effect is the change in the intensity of the DOS spectrum near the Fermi level, which results from modifications in the band gap due to tensile or compressive strain. Figure S1 [in Supporting data file] presents the DOS spectra within a narrower energy range near the Fermi level. The findings reveal that tensile strain slightly increases the zero-intensity region in the DOS spectrum, while compressive strain markedly reduces it. These behaviors are associated with band gap modifications under strain [inset Fig. 2(b)], and our calculated values align well with previous DFT studies[37]. The findings suggest that tensile and compressive strain have markedly different impacts on the electrical properties of BAs, with compressive strain exhibiting more pronounced effects. These results could be valuable in the design and fabrication of BAs-based electronic devices.

To investigate the effects of strain on the optical properties of BAs, the behavior of the real and imaginary parts of the dielectric function are shown in Figs. 3 and 4 for different values of tensile and compressive strain. In the absence of strain, the Im[ε(ω)] spectrum exhibits two distinct peaks in the Near-Infrared (NIR) and ultraviolet (UV) energy range, at approximately 1.2 eV and 3.4 eV. The first peak corresponds to optical transitions from the valence band maximum (VBM) to the conduction band minimum (CBM) at the K point in the Brillouin zone, with its energy directly related to the band gap value. The second peak is associated with optical transitions at the M point, and its position is more sensitive to the strain parameter. By applying strain, the positions of K and M points change, leading to modifications in the |D| function and consequently affecting the optical spectrum.

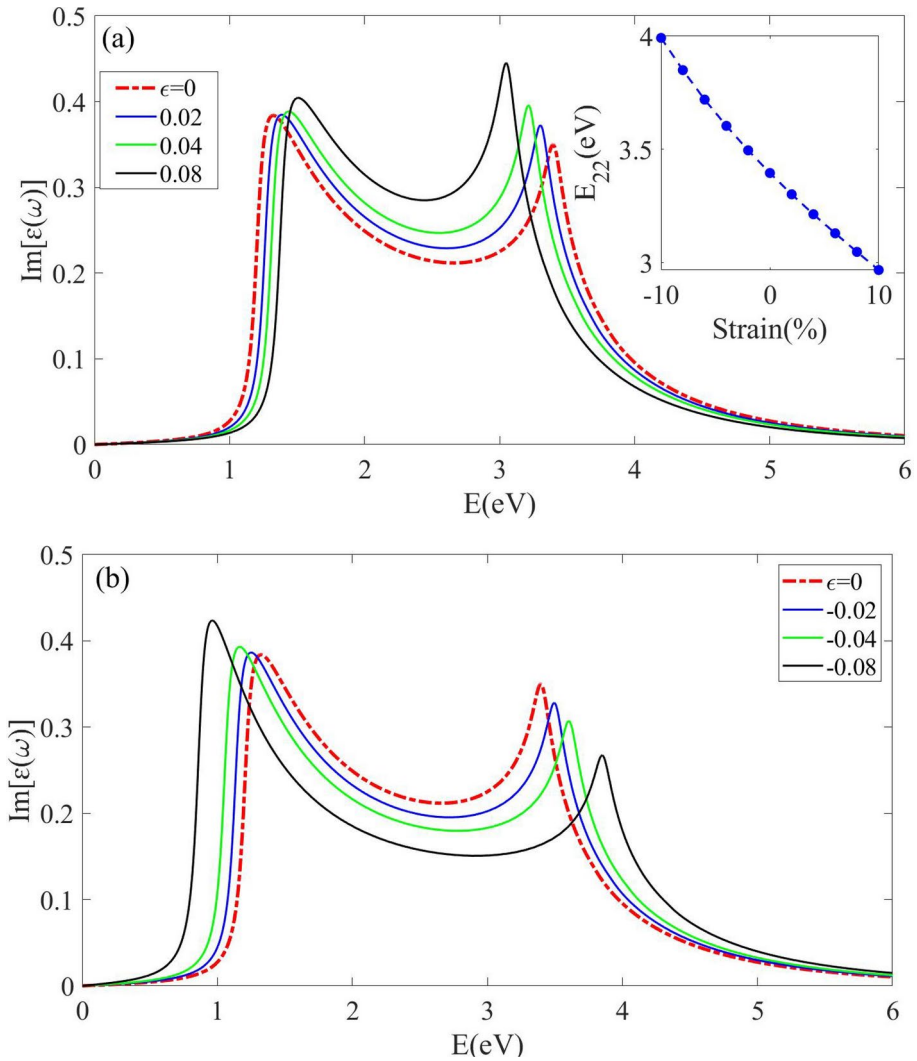

Fig. 3. Imaginary part of the dielectric function Im[ε(ω)] under different (**a**) tensile and (**b**) compressive strain values, showing peaks in the infrared (IR) and ultraviolet (UV) regions. Tensile strain induces a blue-shift and compressive strain demonstrating a red-shift in peak positions increasing energy.

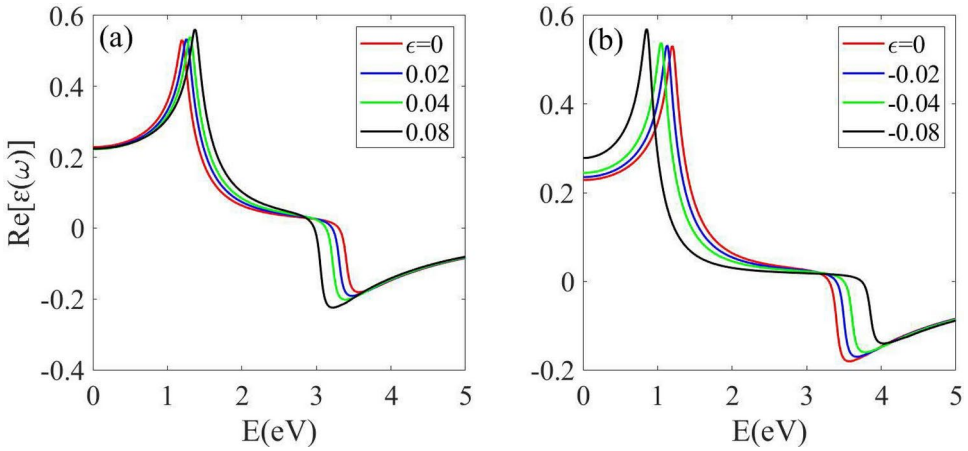

Fig. 4. Real part of the dielectric function Re[ε(ω)] under (**a**) tensile and (**b**) compressive strain.

The results in Fig. 3(a) demonstrate that applying tensile strain leads to a blue shift in the first peak and a red shift in the second peak of the Im[ε(ω)] spectrum, with the magnitude of change being more pronounced for the second peak. Specifically, the second peak shifts to energies of 3.31 eV and 3.05 eV under tensile strains of + 4% and + 12%, respectively. The inset in Fig. 3(a) illustrates the relationship between the strain parameter and the position of the second peak. The results in Fig. 3(b) indicate that the application of compressive strain also alters the position and intensity of the peaks in the Im[ε(ω)] spectrum. These effects include a blue shift for the first peak and a red shift for the second peak, such that unlike tensile strain, the distance between these two peaks increases with compressive strain. For instance, under a compressive strain of − 12%, the Im[ε(ω)] spectrum shows the lowest and highest energy positions for the first and second peaks, respectively. These findings are in excellent agreement with the peak positions obtained from DFT calculations.

Figure 4(a) and (b) shows the behavior of the Re[ε(ω)], for different values of tensile and compressive strain, respectively. In the absence of strain, the Re[ε(ω)] spectrum has two prominent peaks and their positions depend on the strain parameter. These peaks can exhibit red shift (for the first peak under tensile strain and the second peak under compressive strain) and blue shift (for the first peak under compressive strain and the second peak under tensile strain). An important aspect of studying Re[ε(ω)] is the evaluation of the changes in the static dielectric constant, which is determined from the magnitude of Re[ε(ω)] at ω = 0. The finding results in Fig. 4 show that this quantity has negligible changes under tensile strain, while it significantly increases under compressive strain. This behavior is attributed to the enhanced intensity of the Re[ε(ω)] spectrum in the energy range below the first peak.

Figure 5 illustrates the effects of strain on the refractive index n(ω) and compares these results with those obtained from DFT calculations. According to Eq. 7, the behavior of this function depends on the behavior of the real and imaginary parts of the dielectric function. As illustrated in Fig. 5(a) and (b), the position and intensity of the peaks in the n(ω) spectrum are strain-dependent, with more pronounced changes observed under tensile strain. Specifically, tensile strain causes a red-shift in the first peak and a blue-shift in the second peak, whereas compressive strain induces the opposite effect, leading to a blue-shift in the first peak and a red-shift in the second peak.

For a detailed comparison between the tight-binding model used in this study and the DFT results, the n(ω) spectrum is presented over an energy range of 2 eV for different strain values [Fig. 5(c)-(e)]. From the obtained results, it can be observed that at the selected strains, the peak position of the n(ω) spectrum is the same in both models, indicating the accuracy of the tight-binding model used in this study. Additionally, both models show minor differences in the magnitude of n(ω) at ω = 0. It is important to note that the greater intensity observed in the n(ω) spectrum for the tight-binding model compared to the DFT results is due to the smaller broadening parameter used in the corresponding formula.

The optical observations indicate that the optical properties of monolayer BAs are significantly influenced by the application of mechanical strain, leading to shifts in peak positions and variations in spectrum intensity. These effects are more pronounced under compressive strain compared to tensile strain.

As demonstrated in Fig. 6, beyond linear optical properties, the strain parameter can induce significant changes in the quadratic electronic optic (DC Kerr) effect of monolayer BAs. This effect, denoted as $\chi^{(3)}(\omega) \equiv \chi^{(3)}(-\omega, 0, 0, \omega)$, is proportional to the imaginary part of the electric susceptibility. The spectrum of $\chi^{(3)}(\omega)$ shows minimal intensity, approaching zero, in energy regions significantly below the resonance peak. Near the band gap E_g, the intensity of $\chi^{(3)}(\omega)$ increases, reaching a positive peak at an energy slightly below E_g, then exhibits a negative resonance peak at E_g, followed by the formation of another distinct positive peak beyond this point. This observed behavior in the $\chi^{(3)}(\omega)$ spectrum directly arises from the allowed optical transitions at the band edges at the K point. Additionally, a similar pattern is observed in the $\chi^{(3)}(\omega)$ spectrum in the intermediate energy range around 3 eV.

This pattern is evident for all selected conditions with tensile and compressive strain across different energy regions. As shown in Fig. 6(a) and (b), when compressive strain is applied, the first peak exhibits a slight blue

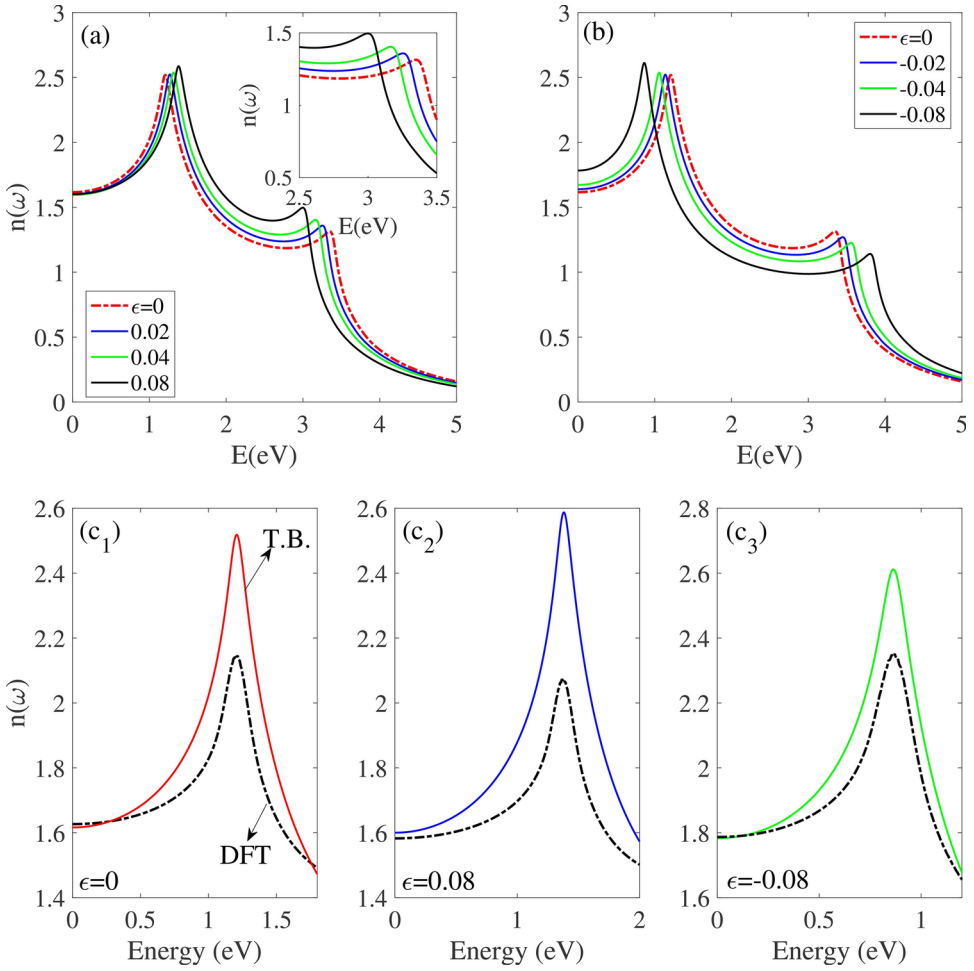

Fig. 5. Refractive index n(ω) under (**a**) tensile and (**b**) compressive strain. (**c**)–(**e**) Comparison of n(ω) between tight-binding and DFT for various strains.

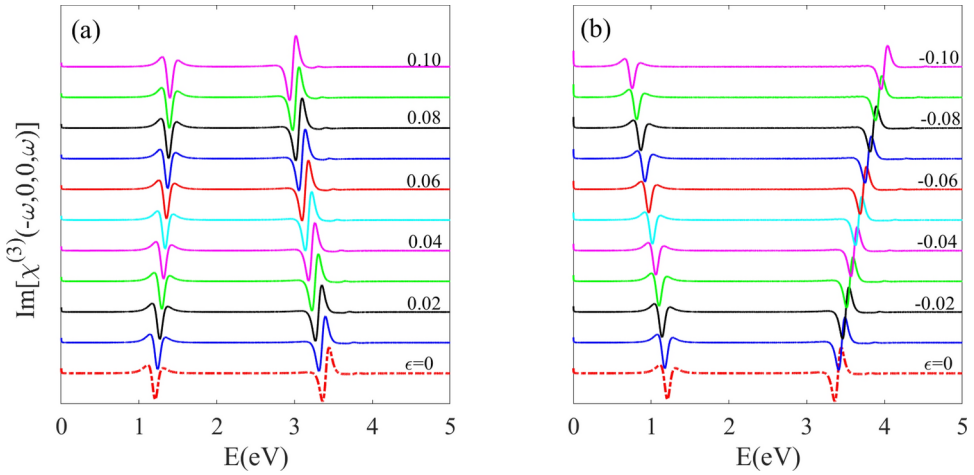

Fig. 6. Quadratic electro-optic (DC Kerr) effect spectrum under (**a**) tensile and (**b**) compressive strain.

shift (corresponding to the increased band gap energy), while the second peak experiences a red shift. The magnitude of these peak shifts increases with the strain, leading to a reduced distance between them. Under tensile strain, the opposite effect is observed, where the first peak shows a red shift and the second peak shows a noticeable blue shift, with the distance between them increases as the strain parameter rises. It can be concluded

that tensile strain has a more pronounced effect on modifying the $\chi^{(3)}(\omega)$ spectrum. The ability to tune these modifications, including changes in sign and resonance characteristics through the application of strain, is of great importance for optimizing and enhancing the performance of electro-optic devices.

Thermoelectric properties

Figures 7, 8 and 9 examine the thermoelectric properties of monolayer BAs in terms of chemical potential, across at temperatures and strain parameters.

Figure 7 illustrates the effects of tensile and compressive strain on the thermal conductivity k(μ) of monolayer BAs at different temperatures. The results indicate that in the absence of strain [Fig. 7(a)], k(μ) exhibits a zero-intensity region within the range μ < 0.5 eV, followed by a linear increase beyond this range. This zero-intensity region arises due to the non-zero band gap in monolayer BAs, which acts as a potential barrier, preventing the excitation of charge carriers to higher energy levels. The width of this zero-intensity region is temperature-dependent, decreasing as the temperature increases, with the minimum observed around 1200 K. This behavior can be attributed to the increased thermal energy of charge carriers at higher temperatures, enabling them to gain sufficient energy for excitation to higher levels at lower μ values. Consequently, the thermal conductivity k(μ) becomes non-zero at smaller μ values and exhibits a steeper slope as temperature rises.

Figure 7(b) and (c) illustrates the effects of tensile and compressive strain on the thermal conductivity of monolayer BAs at temperatures of 300 K and 900 K. The results reveal that at 300 K, a zero-intensity region exists in k(μ) for all selected strain values, though its extent varies depending on the magnitude and type of strain. Under compressive strain, k(μ) becomes non-zero at smaller μ values, while tensile strain broadens the zero-intensity region in k(μ). Another significant finding is the increasing rate of k(μ) with respect to chemical potential, which is more pronounced for compressive strain. Additionally, the intensity of k(μ) reaches its maximum under compressive strain at a magnitude of − 0.08 and its minimum under tensile strain at a magnitude of + 0.08 across the entire μ range.

This behavior pattern remains consistent even at higher temperatures, such as 900 K, regardless of temperature variations. This phenomenon can be explained by considering the dependency of the band gap energy and carrier concentration on strain parameters and μ, respectively. As the chemical potential increases, the carrier concentration also rises, allowing more carriers to be excited to higher energy levels, especially as temperature increases. The reduction in band gap energy under compressive strain intensifies this effect, allowing carrier excitation at lower μ values. These results suggest that the thermal conductivity k(μ) of monolayer BAs is significantly influenced by strain and temperature, with compressive strain leading to notably enhanced conductivity.

Figure 8 illustrates the dependence of the Lorentz number L(μ) and power factor PF(μ) on the parameter μ under tensile and compressive strain. As shown in the Fig. 8(a), in the absence of strain and at 300 K, the L(μ) function exhibits two nearly symmetric peaks in the positive and negative μ regions, with negligible intensity between these peaks. As temperature increases, the peaks shift towards μ = 0, resulting in a symmetric peak with high intensity at μ = 0. The intensity of this peak decreases with increasing temperature. This behavior occurs because, at 300 K, the thermal energy is not sufficiently high to excite charge carriers in the small μ range.

As shown in the Fig. 8(b), applying tensile or compressive strain has different effects on L(μ). At 900 K, tensile strain decreases the intensity of L(μ) around μ = 0, while compressive strain increases it. At this temperature, the strain value of ± 0.08 leads to the highest and lowest intensities of L(μ), respectively. The behavior of L(μ) at higher temperatures follows a similar pattern, but at lower temperatures, it exhibits different characteristics. As shown in inset Fig. 8(b), at 300 K, the application of strain shifts the L(μ) peaks within the ± μ range, with compressive strain bringing the peaks closer together, while tensile strain moves them farther apart.

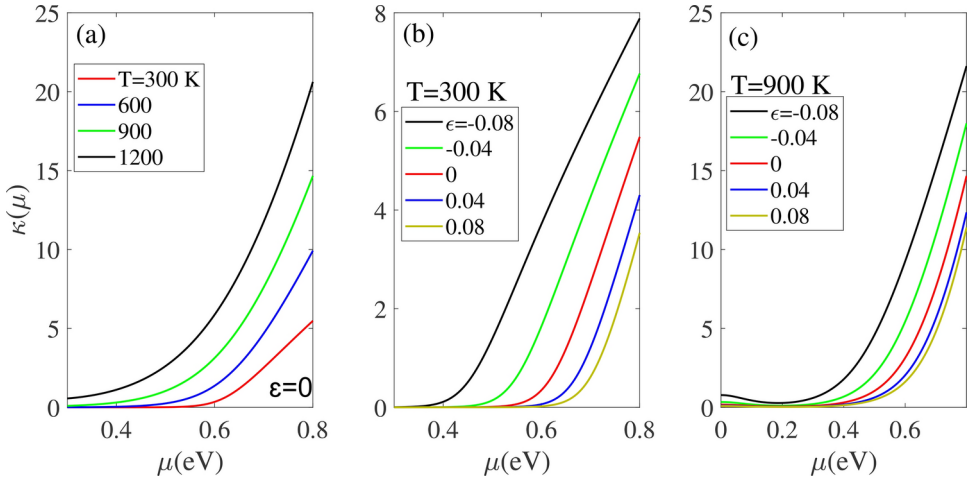

Fig. 7. (**a**) Thermal conductivity at different temperatures, showing zero intensity in the small chemical potential range, increasing linearly at higher μ. (**b**) and (**c**) k(μ) under tensile and compressive strains, respectively. Tensile strain broadening the zero-intensity range and compressive strain reducing it.

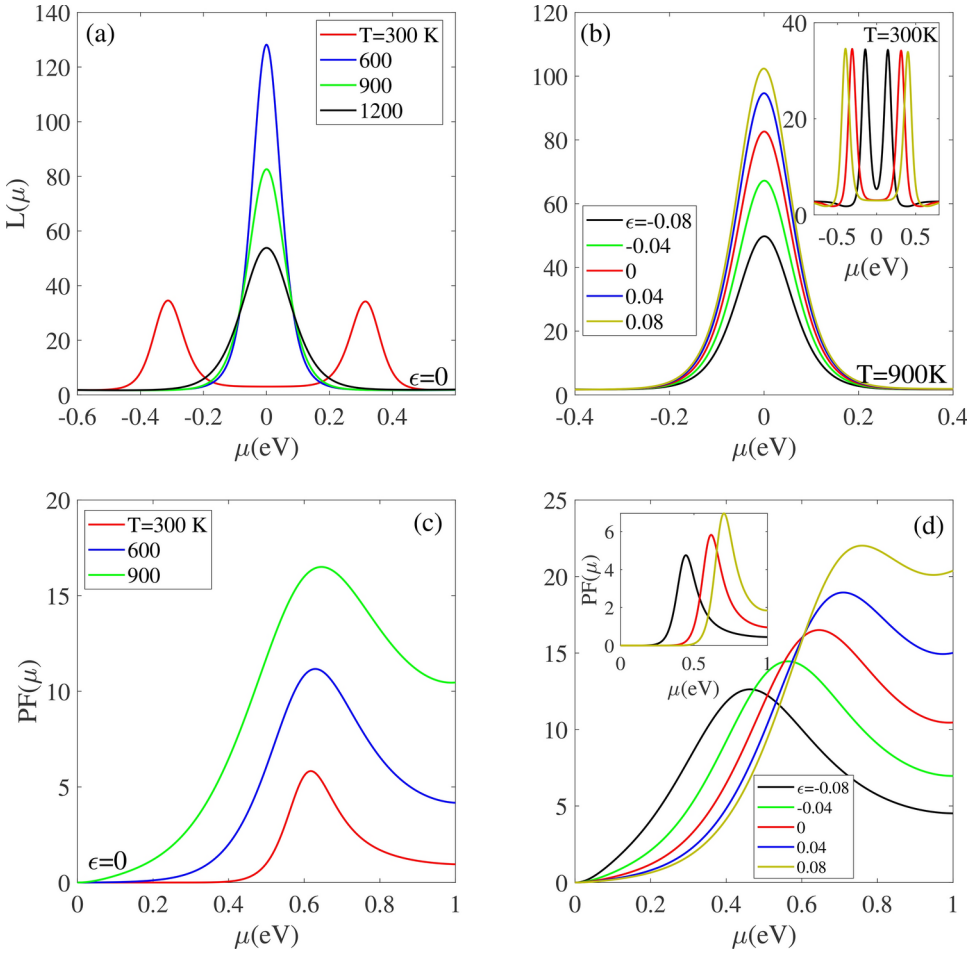

Fig. 8. The dependence of the Lorentz number L(μ) on the parameter μ under different values of (**a**) temperature and (**b**) tensile and compressive strain, respectively. The dependence of the power function PF(μ) on the parameter μ under different values of (**a**) temperature and (**b**) tensile and compressive strain, respectively.

Figure 8(c) and (d) shows the behavior of PF(μ) as a function of μ under different strain and temperature values. At 300 K and without strain, PF(μ) has zero intensity in the μ < 0.4 eV range and then increases, reaching a peak at μ = 0.6 eV. The intensity of PF(μ) is directly related to temperature, with higher temperatures causing PF(μ) to begin increasing at a smaller μ and its magnitude rising with a steeper slope. For instance, at 600 K, PF(μ) starts to rise at μ > 0.2 eV and reaches a peak at μ = 0.6eV. This effect is more pronounced at 900 K. The effects of strain on PF(μ) at 900 K, as shown in Fig. 8(d), reveal that tensile strain increases the intensity of PF(μ) and shifts the peak towards larger μ values. Conversely, compressive strain decreases the intensity of PF(μ) and shifts the peak to lower μ values. For instance, compressive strain results in the lowest intensity at μ = − 0.08, with the peak occurring at a smaller μ compared to other strain values.

Figure 9 illustrates the behavior of the Seebeck coefficient S(μ) under various temperature and strain conditions. At 300 K, the S(μ) function exhibits a zero value around μ = 0, followed by positive and negative peaks for ± μ values, respectively [Fig. 9(a)]. As the temperature increases to 600 K, these peaks shift towards μ = 0 and the zero-intensity range disappears. This pattern persists at higher temperatures, such as 900 K and 1200 K, where the intensity of the peaks in the S(μ) function decreases with rising temperature. Figure 9(b) shows the effect of tensile and compressive strain on S(μ) at 300 K and 900 K. At 300 K, for all selected strain values, S(μ) maintains a zero-intensity range around μ = 0, with the size of this range depending on the magnitude and direction of the strain [inset Fig. 9(b)]. For instance, applying tensile strain increases the size of this zero-intensity range, causing the S(μ) peaks to shift towards larger μ values on both sides of μ = 0. In contrast, compressive strain reduces the zero-intensity range and shifts the peaks towards μ = 0. At 900 K, the S(μ) function exhibits a different pattern without a zero-intensity region. In this case, the intensity of the peaks increases with tensile strain and decreases with compressive strain.

Conclusions

In conclusion, this study provides a detailed theoretical exploration of the effects of tensile and compressive strain on the electronic, optical, and thermoelectric properties of monolayer BAs, using a tight-binding model

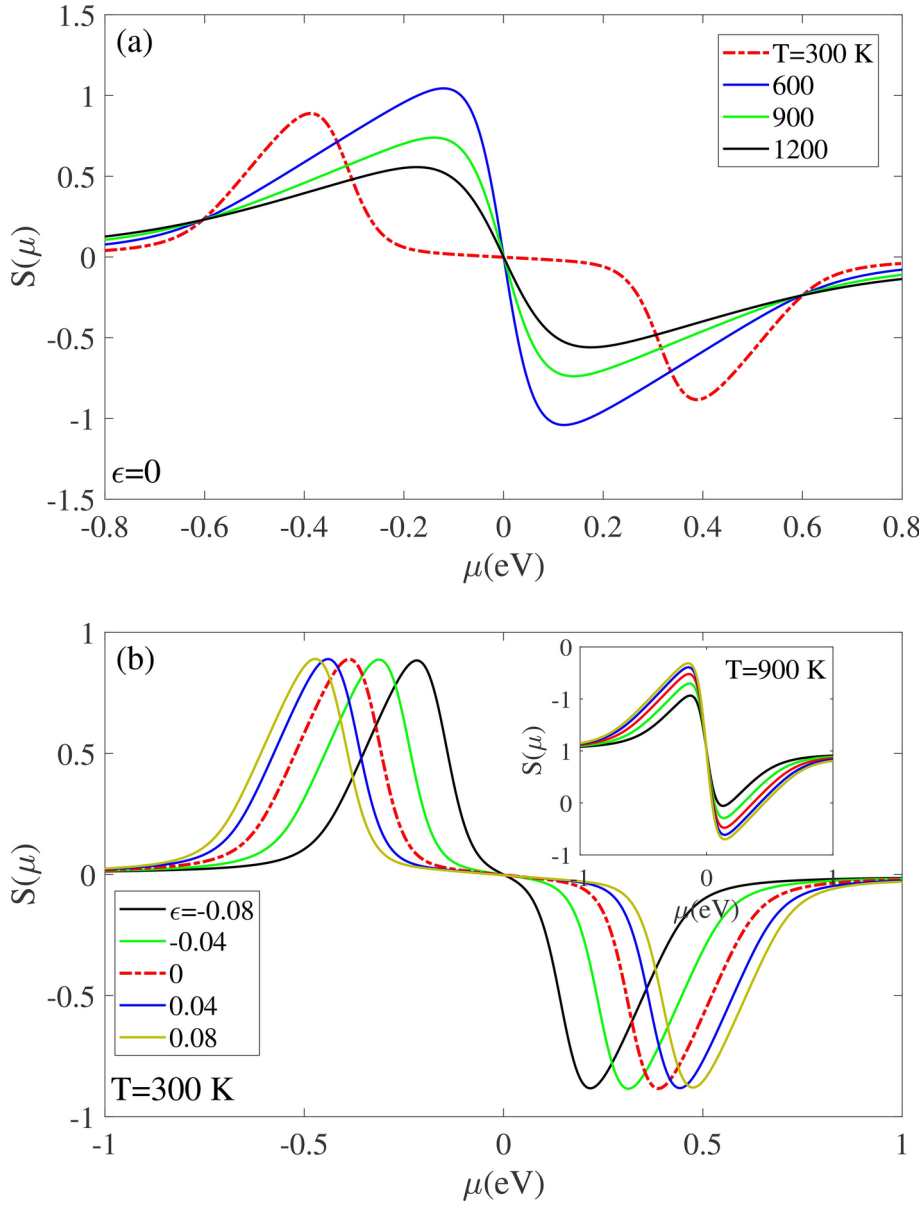

Fig. 9. Behavior of the Seebeck coefficient S(μ) under various (**a**) temperature and (**b**) strain conditions.

parameterized by DFT calculations. The results reveal that monolayer BAs maintains its semiconducting properties within a strain range of −8% to +8%, with compressive strain reducing the band gap and tensile strain increasing it. This band gap modulation leads to notable changes in the DOS spectra and impacts the allowed electronic transitions. The optical response of monolayer BAs is characterized by two primary peaks in the IR and UV regions, corresponding to transitions at the K and M points in the Brillouin zone. The optical peaks are sensitive to strain, with compressive strain causing a red-shift and tensile strain resulting in a blue-shift, presenting promising mechanisms for tailoring the optical properties of BAs-based optoelectronic devices. Furthermore, strain-induced band gap configurations also significantly affect the thermoelectric performance of BAs, with compressive strain increasing the thermal conductivity and Seebeck coefficient, while tensile strain generally decreases these properties. Overall, this study highlights the potential of strain engineering as a powerful tool to optimize BAs monolayers for applications in advanced thermoelectric and optoelectronic devices, providing insights into the adaptable material properties under strain.

Data availability

The datasets used and analyzed during the current study available from the corresponding author on reasonable request.

Received: 4 November 2024; Accepted: 18 April 2025

Published online: 09 May 2025

References

1. Ahn, E. C. 2D materials for spintronic devices. *NPJ 2D Mater. Appl.* **4**(1), 17 (2020).
2. Zhang, Y. et al. Advanced optical polarizers based on 2D materials. *NPJ Nanophotonics* **1**(1), 28 (2024).
3. Ma, Q. et al. Tunable optical properties of 2D materials and their applications. *Adv. Opt. Mater.* **9**(2), 2001313 (2021).
4. Urade, A. R., Lahiri, I. & Suresh, K. Graphene properties, synthesis and applications: A review. *JOM* **75**(3), 614–630 (2023).
5. Mbayachi, V. B. et al. Graphene synthesis, characterization and its applications: A review. *Results Chem.* **3**, 100163 (2021).
6. Liu, J., Bao, S. & Wang, X. Applications of graphene-based materials in sensors: A review. *Micromachines* **13**(2), 184 (2022).
7. Zhen, Z. & Zhu, H. Structure and properties of graphene. In *Graphene* 1–12 (Elsevier, 2018).
8. Castro Neto, A. H. et al. The electronic properties of graphene. *Rev. Mod. Phys.* **81**(1), 109–162 (2009).
9. Novoselov, K. S. et al. Two-dimensional gas of massless Dirac fermions in graphene. *Nature* **438**(7065), 197–200 (2005).
10. Park, C.-H. et al. New generation of massless Dirac fermions in graphene under external periodic potentials. *Phys. Rev. Lett.* **101**(12), 126804 (2008).
11. Sahu, S. & Rout, G. Band gap opening in graphene: A short theoretical study. *Int. Nano Lett.* **7**, 81–89 (2017).
12. Rani, P. & Jindal, V. Designing band gap of graphene by B and N dopant atoms. *RSC Adv.* **3**(3), 802–812 (2013).
13. Dean, C. et al. Graphene based heterostructures. *Solid State Commun.* **152**(15), 1275–1282 (2012).
14. Si, C., Sun, Z. & Liu, F. Strain engineering of graphene: A review. *Nanoscale* **8**(6), 3207–3217 (2016).
15. Chegel, R., Behzad, S. & Ahmadi, E. Effects of electric and magnetic fields on the electronic properties of zigzag carbon and boron nitride nanotubes. *Solid State Sci.* **14**, 456–464. https://doi.org/10.1016/j.solidstatesciences.2012.01.014 (2012).
16. Chegel, R. Theoretical investigation of enhanced nonlinear optical properties of silicene and carbon nanotubes: Potential applications in infrared and ultraviolet optoelectronics. *J. Lumin.* **277**, 120923 (2025).
17. Liu, L. & Shen, Z. Bandgap engineering of graphene: A density functional theory study. *Appl. Phys. Lett.* **95**(25), 6068 (2009).
18. Chaves, A. et al. Bandgap engineering of two-dimensional semiconductor materials. *NPJ 2D Mater. Appl.* **4**(1), 29 (2020).
19. Zia, A. et al. MXene, silicene and germanene: Preparation and energy storage applications. *Mater. Today Energy* **30**, 101144 (2022).
20. Chegel, R. & Behzad, S. Tunable electronic, optical, and thermal properties of two- dimensional Germanene via an external electric field. *Sci. Rep.* **10**(1), 704 (2020).
21. Roy, S. et al. Structure, properties and applications of two-dimensional hexagonal boron nitride. *Adv. Mater.* **33**(44), 2101589 (2021).
22. Mondal, R. et al. Electronic and transport property of two-dimensional boron phosphide sheet. *J. Mol. Graph. Model.* **112**, 108117 (2022).
23. Chabi, S. et al. The creation of true two-dimensional silicon carbide. *Nanomaterials* **11**(7), 1799 (2021).
24. Shi, Z. et al. Predicting two-dimensional silicon carbide monolayers. *ACS Nano* **9**(10), 9802–9809 (2015).
25. Chegel, R. Bias induced modulation of electrical and thermal conductivity and heat capacity of BN and BN/graphene bilayers. *Phys. B: Condens. Matter* **511**, 26–35. https://doi.org/10.1016/j.physb.2017.01.031 (2017).
26. Ni, Z. et al. Tunable Bandgap in Silicene and Germanene. *Nano Lett.* **12**(1), 113–118 (2012).
27. Schwierz, F., Pezoldt, J. & Granzner, R. Two-dimensional materials and their prospects in transistor electronics. *Nanoscale* **7**(18), 8261–8283 (2015).
28. Drummond, N., Zolyomi, V. & Fal'Ko, V. Electrically tunable band gap in silicene. *Phys. Rev. B Condens. Matter Mater. Phys.* **85**(7), 075423 (2012).
29. Alfieri, G. & Kimoto, T. The structural and electronic properties of chiral SiC nanotubes: A hybrid density functional study. *Nanotechnology* **20**(28), 285703 (2009).
30. Liu, B., Abbas, A. & Zhou, C. Two-dimensional semiconductors: From materials preparation to electronic applications. *Adv. Electron. Mater.* **3**(7), 1700045 (2017).
31. Hu, Y. et al. High thermal conductivity driven by the unusual phonon relaxation time platform in 2D monolayer boron arsenide. *RSC Adv.* **10**(42), 25305–25310 (2020).
32. Mohanta, M. K. & De Sarkar, A. Giant tunability in electrical contacts and doping via inconsiderable normal electric field strength or gating for a high-performance in ultrathin field effect transistors based on 2D BX/graphene (X = P, As) van der Waals heterobilayer. *Appl. Surf. Sci.* **526**, 146749 (2020).
33. Şahin, H. et al. Monolayer honeycomb structures of group-IV elements and III-V binary compounds: First-principles calculations. *Phys. Rev. B* **80**(15), 155453 (2009).
34. Zhuang, H. L. & Hennig, R. G. Electronic structures of single-layer boron pnictides. *Appl. Phys. Lett.* **101**(15), 8465 (2012).
35. Zhang, X. et al. The electron–phonon scattering and charge transport of the two-dimensional (2D) polar h-BX(X = P, As, Sb) monolayers. *New J. Phys.* **25**(12), 123043 (2023).
36. Khossossi, N. et al. Ab initio study of a 2D h-BAs monolayer: A promising anode material for alkali-metal ion batteries. *Phys. Chem. Chem. Phys.* **21**(33), 18328–18337 (2019).
37. Islam, R. et al. Tuning the electronic, phonon, and optical properties of monolayer BX (XP and As) through the strain effect. *Mater. Today Commun.* **33**, 104227 (2022).
38. Khurami, M. W. et al. Strain engineering on structural, optoelectronic and photocatalytic properties of BP, BAs and BSb monolayers. *Solid State Commun.* **371**, 115273 (2023).
39. Behzad, S. & Chegel, R. Investigation of effects of interlayer interaction and biaxial strain on the phonon dispersion and dielectric response of hexagonal boron arsenide. *Sci. Rep.* **13**(1), 21339 (2023).
40. Sharma, S. B. et al. Strain dependent electronic and optical responses of penta-BCN monolayer. *Carbon Trends* **7**, 100162 (2022).
41. Luo, M. & Xu, Y. E. Tunable band-gap of the GeC monolayer by strain and electric field: A first-principles study. *Optik* **195**, 163147 (2019).
42. Xu, Z., Li, Y. & Liu, Z. Controlling electronic and optical properties of layered SiC and GeC sheets by strain engineering. *Mater. Des.* **108**, 333–342 (2016).
43. Shu, H. & Guo, J. Enhanced stability and tunable optoelectronic properties of silicon–carbon monolayers by strain and surface functionalization. *J. Mater. Chem. C* **12**(16), 5916–5925 (2024).
44. Shu, H., Guo, J. & Niu, X. Electronic, photocatalytic, and optical properties of two-dimensional boron pnictides. *J. Mater. Sci.* **54**(3), 2278–2288 (2019).
45. Shu, H. & Guo, J. Strain effects of stability, transport, and electro-optical properties of novel Ga2TeS monolayer. *J. Mater. Sci.* **59**(6), 2403–2415 (2024).
46. Shu, H. Adjustable electro-optical properties of novel graphene-like SiC2 via strain engineering. *Appl. Surf. Sci.* **559**, 149956 (2021).
47. Shahriar, R. et al. Vacancy induced magnetism and electronic structure modification in monolayer hexagonal boron arsenide: A first-principles study. *Appl. Surf. Sci.* **600**, 154053 (2022).
48. Helal, M. A. & Fadlallah, M. M. Structural, electronic, magnetic and optical properties of transition metal doped boron arsenide nanosheets. *Phys. Scr.* **99**(2), 025904 (2024).
49. Li, Z. et al. Monolayer hexagonal arsenene with tunable electronic structures and magnetic properties via impurity doping. *J. Mater. Chem. C* **4**(2), 362–370 (2016).

50. Ullah, S., Denis, P. A. & Sato, F. Monolayer boron-arsenide as a perfect anode for alkali-based batteries with large storage capacities and fast mobilities. *Int. J. Quantum Chem.* **119**(18), e25975 (2019).
51. Ranjan, P. et al. Enhanced optoelectronic traits of monolayer h-BAs for augmented NOx (NO and NO_2) Gas Sensing. *IEEE Sens. J.* **24**(13), 20504–20511 (2024).
52. Ren, J., Kong, W. & Ni, J. The potential application of BAs for a gas sensor for detecting SO_2 gas molecule: A DFT study. *Nanoscale Res. Lett.* **14**(1), 133 (2019).
53. Khanh Nguyen, D. et al. Surface functionalization of graphene-like boron arsenide monolayer: A first-principles study. *J. Phys. Condens. Matter* **36**(5), 055001 (2024).
54. Manoharan, K. & Subramanian, V. Exploring multifunctional applications of hexagonal boron arsenide sheet: A DFT study. *ACS Omega* **3**(8), 9533–9543 (2018).
55. Fayaz, M. et al. Tunable optoelectronic and photocatalytic properties of BAs-BSe van der Waals heterostructures by strain engineering. *Chem. Phys.* **565**, 111769 (2023).
56. Dai, X., Zhang, X. & Li, H. Semiconductor-metal transition in multi-layer sandwiched BAs/BP heterostructures induced by BP intercalation. *Appl. Surf. Sci.* **507**, 144923 (2020).
57. Ye, H. et al. Strain and electric field tuned electronic properties of BAs/MoSe2 van der Waals heterostructures for alternative electrodes and photovoltaic cell in photocatalysis. *Physica E* **120**, 114055 (2020).
58. Charlier, A. et al. Metal–semiconductor transitions under uniaxial stress for single- and double-walled carbon nanotubes. *J. Phys. Chem. Solids* **62**(3), 439–444 (2001).
59. Mortezaei Nobahari, M. Electro-optical properties of strained monolayer boron phosphide. *Sci. Rep.* **13**(1), 9849 (2023).
60. Verberck, B. et al. Strain-induced band gaps in bilayer graphene. *Phys. Rev. B Condens. Matter Mater. Phys.* **85**(12), 125403 (2012).
61. Jiang, J. et al. Optical absorption matrix elements in single-wall carbon nanotubes. *Carbon* **42**(15), 3169–3176 (2004).
62. Zarifi, A. & Pedersen, T. G. Universal analytic expression of electric-dipole matrix elements for carbon nanotubes. *Phys. Rev. B* **80**(19), 195422 (2009).
63. Matsubara, M. et al. Optimal thermoelectric power factor of narrow-gap semiconducting carbon nanotubes with randomly substituted impurities. *J. Phys. Soc. Jpn.* **90**(4), 044702 (2021).
64. Behzad, S. Strategies to optimize the intricate thermoelectric properties of 2D tetragonal silicene for energy harvesting: A computational modeling approach. *Appl. Phys. A* **130**(5), 288 (2024).
65. Joura, A. V., Demchenko, D. O. & Freericks, J. K. Thermal transport in the Falicov-Kimball model on a Bethe lattice. *Phys. Rev. B* **69**(16), 165105 (2004).

Author contribution
R. Chegel carried out the idea and performed the calculations.

Funding
Not applicable.

Declarations

Competing interests
The author declares no competing interests.

Additional information
Supplementary Information The online version contains supplementary material available at https://doi.org/10.1038/s41598-025-99320-1.

Correspondence and requests for materials should be addressed to R.C.